

Lattice Mismatch-Driven In-Plane Strain Engineering for Enhanced Upper Critical Fields in Mo₂N Superconducting Thin Films

Aditya Singh, Divya Rawat, Victor Hjort, Abhisek Mishra, Arnaud le Febvrier, Subhankar Bedanta, Per Eklund,* and Ajay Soni*

Transition metal nitrides are a fascinating class of hard coating material that provides an excellent platform for investigating superconductivity and fundamental electron-phonon (*e-ph*) interactions. In this work, the structural, morphological, and superconducting properties have been studied for Mo₂N thin films deposited via direct current magnetron sputtering on *c*-plane Al₂O₃ and MgO substrates to elucidate the effect of internal strain on superconducting properties. High-resolution X-ray diffraction and time-of-flight elastic recoil detection analysis confirm the growth of single-phase Mo₂N thin films exhibiting epitaxial growth with twin-domain structure. Low-temperature electrical transport measurements reveal superconducting transitions at ≈ 5.2 and ≈ 5.6 K with corresponding upper critical fields of ≈ 5 and ≈ 7 T for the films deposited on Al₂O₃ and MgO, respectively. These results indicate strong type-II superconductivity, and the observed differences in superconducting properties are attributed to substrate-induced strain, which leads to higher *e-ph* coupling for the film on MgO substrate. These findings highlight the tunability of superconducting properties in Mo₂N films through strategic substrate selection.

quantum interference devices, and quantum computing.^[1,2] The ability to tune the superconductivity in epitaxial thin films, in comparison to the bulk counterparts, enables precise control over critical parameters such as carrier density, conformality to curved surfaces, thus allowing functionalities like manipulation of magnetic flux and switching in Josephson junctions.^[3] Among the various material systems explored for thin film functionalities, the Transition Metal Nitrides (TMNs) stand out due to their multidisciplinary array of technological applications arising from their thermal stability, refractory character, and chemical resistance.^[4–6] Epitaxial growth of thin films of TMNs on various substrates allows for precise control of morphology and structures at the atomic-level, further enhancing their potential for advanced quantum technologies. TMNs display a range of functional properties,

1. Introduction

Superconductivity in thin films has garnered significant attention due to their well-defined geometry, enhanced surface-to-volume ratio, and remarkable sensitivity to external stimuli, making them ideal candidates for a diverse technological applications, including single-photon detectors, superconducting

including superconductivity,^[7,8] quantum magnetism,^[9,10] exceptional hardness^[11–13] making them suitable for applications in electronics, energy storage, photocatalysis, supercapacitor electrodes, and beyond.^[5,13]

Within the TMN family, niobium, scandium, and titanium nitrides have been widely studied for their superconducting behavior, thermal management, and compatibility with

A. Singh, D. Rawat, A. Soni
School of Physical Sciences
Indian Institute of Technology Mandi
Mandi, Himachal Pradesh 175005, India
E-mail: ajay@iitmandi.ac.in

V. Hjort, P. Eklund
Thin Film Physics Division
Department of Physics, Chemistry, and Biology (IFM)
Linköping University
Linköping SE-58183, Sweden
E-mail: per.eklund@kemi.uu.se

A. Mishra, S. Bedanta
Laboratory for Nanomagnetism and Magnetic Materials (LNMM)
School of Physical Sciences
National Institute of Science Education and Research (NISER)
An OCC of Homi Bhabha National Institute (HBNI)
Jatni, Odisha 752050, India

A. le Febvrier, P. Eklund
Department of Chemistry – Ångström Laboratory
Inorganic Chemistry
Uppsala University
Uppsala 75105, Sweden

 The ORCID identification number(s) for the author(s) of this article can be found under <https://doi.org/10.1002/admi.202500586>

© 2025 The Author(s). Advanced Materials Interfaces published by Wiley-VCH GmbH. This is an open access article under the terms of the [Creative Commons Attribution](https://creativecommons.org/licenses/by/4.0/) License, which permits use, distribution and reproduction in any medium, provided the original work is properly cited.

DOI: 10.1002/admi.202500586

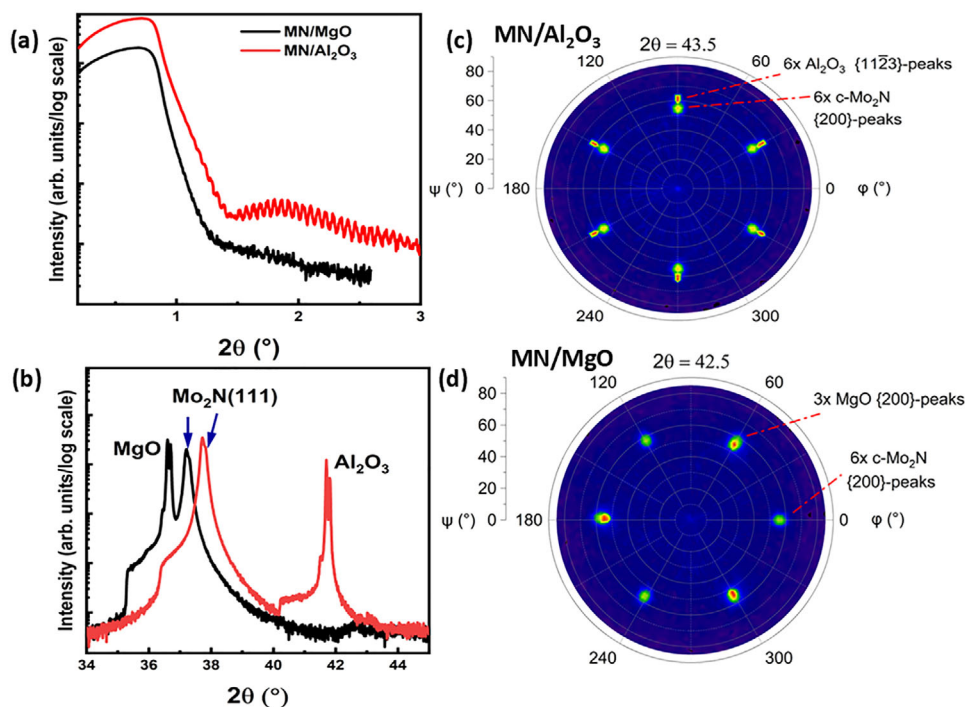


Figure 1. a) XRR plot for MN/Al₂O₃ and MN/MgO (XRR is shifted vertically for visual clarity), b) θ - 2θ XRD patterns. Pole figures indicating single-phase epitaxial growth for c) MN/Al₂O₃ and d) MN/MgO.

device integration.^[14–16] However, molybdenum nitrides (Mo–N) present a more complex case owing to their rich phase diagram, where even minor changes in temperature or nitrogen content can lead to multiple competing phases.^[17] Previous research on Mo₂N_x systems has explored the impact of nitrogen and argon content in the plasma during the sputtering on the superconducting properties,^[18] magnetization behavior of different Mo₂N_x phases,^[19] thickness-dependent superconducting properties of polycrystalline Mo₂N films grown on AlN-buffered Si substrates,^[20] surface-induced suppressed superconductivity using low-temperature tunnelling spectroscopy.^[21] The performance of these films is limited by either the formation of different Mo–N phases that coexist with Mo₂N or the deviation of Mo₂N from the perfect stoichiometry. Despite these efforts, comprehensive investigations on phase-pure and stoichiometric Mo₂N thin films grown on substrates such as Al₂O₃ (MN/Al₂O₃) and MgO (111) (MN/MgO) are lacking, particularly where the detailed structural and low-temperature studies are involved. Moreover, recent theoretical predictions^[22] using Eliashberg formalism estimate a superconducting critical temperature (T_c) \approx 15.8 K for Mo₂N with a strong e - ph coupling constant of \approx 1.2. These findings highlight the need for experimental validation, particularly since strain induced by lattice mismatch can modify the e - ph interactions and potentially enhance superconducting properties. In general, the in-plane compressive strain flattens the electronic bands, leading to an enhanced density of states near the Fermi energy, thereby elevating the superconducting T_c .^[23]

In this work, we report a detailed study on superconductivity in phase-pure cubic Mo₂N thin films grown on c -plane Al₂O₃ and MgO (111) substrates, via DC reactive magnetron sputter-

ing. The films exhibit a well-defined twin domain structure, as confirmed by X-ray diffraction (XRD) and pole figure analysis. Composition and stoichiometry are determined using Time-of-Flight Elastic Recoil Detection Analysis (ToF-ERDA), affirming near-ideal nitrogen incorporation. [The details are presented in Figure S1, Supporting Information] Temperature-dependent electrical transport measurements reveal superconducting transitions with T_c up to \approx 5.6 K. The upper critical field (H_{c2}) for the MN/MgO shows a significant enhancement (\approx 25%) from MN/Al₂O₃. Despite having the same composition, the enhancement is related to the effect of in-plane compressive strain on the MN/Al₂O₃, which leads to the modulation of Cooper pair formation. Magnetic measurements provide the details of lower critical fields (H_{c1}), coherence lengths, and penetration depths, which support the robust type-II superconducting character of the films. Additionally, the Debye temperature of the thin films is estimated from the fitting of the thermal response of resistance with the Bloch-Grüneisen model, thereby providing a critical insight into e - ph interactions. These results demonstrate that epitaxial MN/MgO can serve as a viable platform for superconducting applications with tunable physical properties.

2. Results and Discussion

The composition of the films is determined from the ERDA (Figure S1 and Table S1, Supporting Information) and found to be Mo₂N_{0.96} and Mo₂N_{0.97} for MN/Al₂O₃ and MN/MgO, respectively, which is very close to the stoichiometric Mo₂N phase, within the error limits. The thickness of the films is estimated by

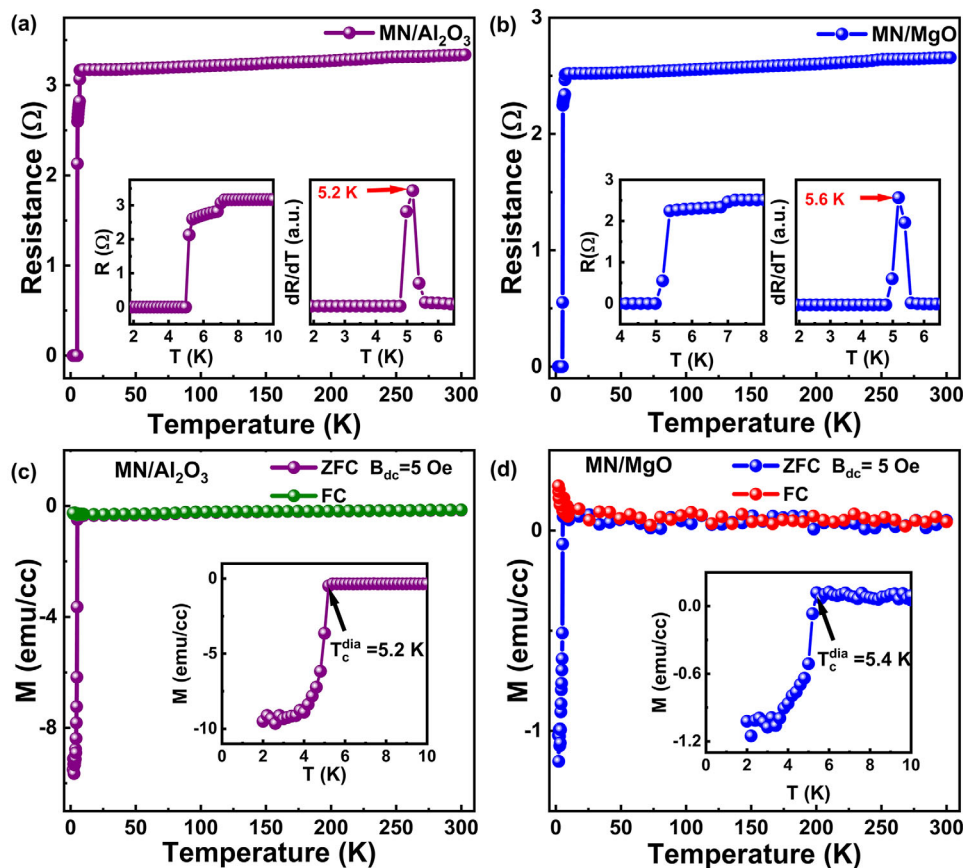


Figure 2. Temperature-dependent resistance of a) MN/Al₂O₃ and b) MN/MgO. The inset shows dR/dT plots for estimation of T_c and temperature-dependent magnetization of c) MN/Al₂O₃ and d) MN/MgO. The T_c in the insets is supporting the observation in transport measurements within the error limits of the techniques.

X-Ray Reflectivity (XRR) (Figure 1a) and is found to be $\approx 130 \pm 5$ nm with estimated roughness of ≈ 2 and ≈ 5 nm for MN/Al₂O₃ and MN/MgO, respectively. The mass density of the films extracted from XRR is presented in Table S1 (Supporting Information). Figure 1b displays the XRD patterns of the two samples, where the substrate peaks for (0001) Al₂O₃ and (111) MgO are visible at $2\theta \approx 41.7^\circ$ (PDF 00-046-1212) and at $2\theta \approx 36.6^\circ$ (PDF 01-071-6452) and are split due to the diffraction coming from the $K_{\alpha 1}$ - $K_{\alpha 2}$ lines, respectively. The peak at $2\theta \approx 37.7^\circ$ (d-spacing 2.38 Å) for MN/Al₂O₃ and $2\theta \approx 37.2^\circ$ (d-spacing 2.42 Å) for MN/MgO corresponds to the (111) plane of cubic Mo₂N with a dominant out-of-plane orientation. The shift in the intense MN-111 peak is because of the substrate-driven stress. The in-plane orientation of the films is further demonstrated by the pole figure analysis of the 200-reflection of Mo₂N, observed at $2\theta \approx 43.5^\circ$ for MN/Al₂O₃ and $\approx 42.5^\circ$ for MN/MgO, as shown in Figure 1c,d. The six poles of Al₂O₃ 11 $\bar{2}$ 3, at $\Psi = 61.5^\circ$ and six poles of c-Mo₂N 200, at $\Psi = 55.5^\circ$ in Figure 1c indicates epitaxial twin-domain growth, a common feature for cubic structures on both the substrates.^[24–26] In Figure 1d, three prominent poles are observed at $\Psi = 54.7^\circ$, corresponding to MgO 200-reflections from the substrate alongside six poles from the Mo₂N (200) planes, spaced every 60° in φ , with some overlapping the MgO poles. Since both MgO and Mo₂N are cubic, their 200 poles are ex-

pected to align at $\Psi = 54.7^\circ$ in a stress-free state. However, the Mo₂N poles appear at a slightly higher $\Psi (\approx 55.5^\circ)$, indicating in-plane compressive strain in the film consistent with observations in Figure 1b. The epitaxial relationship of Mo₂N on both substrates is as follows: (111)_{Mo2N} || (0001)_{Al2O3} (out-of-plane) and [11 $\bar{2}$]_{Mo2N} || [10 $\bar{1}$ 0]_{Al2O3} (in-plane); and (111)_{Mo2N} || (111)_{MgO} (out-of-plane) and [110]_{Mo2N} || [110]_{MgO}. The morphological studies, as well as the AFM images, reveal a smooth surface with voids and grain boundaries, provided in the (Figure S2a–d, Supporting Information).

Comprehensive characterization using ERDA, XRD, and pole figure confirms that both films consist of a single-phase Mo₂N with identical composition. Epitaxial growth is observed on both c-plane Al₂O₃ and MgO (111) substrates, with twin domains present in each case. Despite the consistent composition, a notable shift in the XRD peak positions is observed between the two films, attributed to strain induced by their epitaxial relationship with the respective substrates. Comparing with the XRD peaks of stress-free Mo₂N (37.4°) as a reference, the MN/Al₂O₃ film exhibits a peak shift indicative of in-plane tensile strain, while the MN/MgO film shows a shift consistent with in-plane compressive strain.

The onset of superconductivity in the thin films is estimated from electrical transport and magnetization measurements. The

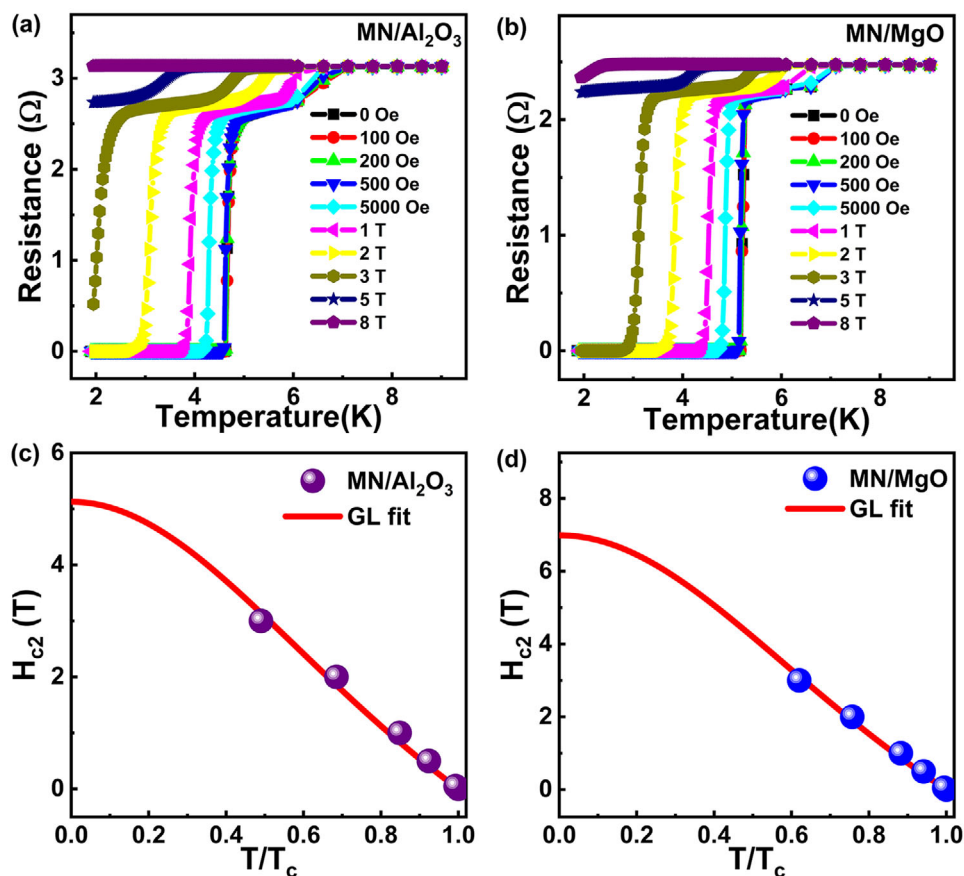


Figure 3. Low temperature magnetoresistance measurements for a) MN/Al₂O₃ and b) MN/MgO. Upper critical field with Ginzburg-Landau fitting of c) MN/Al₂O₃ and d) MN/MgO.

R (300 K) for the films is $\approx 3.33 \Omega$ and $\approx 2.65 \Omega$ for MN/Al₂O₃ and MN/MgO, respectively, which is attributed to the increased grain boundary scattering in the MN/Al₂O₃ as compared to MN/MgO (Figure S2c,d, Supporting Information). In order to study the quality of thin films, the residual resistivity ratio, $RRR = \frac{\rho(300\text{ K})}{\rho(6\text{ K})}$, is calculated for both the thin films, which are found to be ≈ 1.22 for MN/Al₂O₃ and 1.14 for MN/MgO. The significantly higher RRR compared to previously reported Mo₂N thin films on Si substrates ($RRR \approx 0.9$)^[20] indicates a superior crystallinity, reduced defect density, and larger grain sizes with fewer macroscopic imperfections. The R - T data (Figure 2a,b) confirm the metallic nature of the films with the T_c estimated from the derivative plot of resistance (inset of Figure 2a,b), which shows the $T_c \approx 5.2$ K (for MN/Al₂O₃) and $T_c \approx 5.6$ K (for MN/MgO). The estimated T_c is further corroborated by magnetization measurements of the Meissner effect (Figure 2c,d). Magnetization data (M - T) obtained using both field-cooled (FC) and zero-field-cooled (ZFC) protocols exhibit robust diamagnetic behavior with a $T_c^{dia} = 5.2$ K and $T_c^{dia} = 5.4$ K, for MN/Al₂O₃ and MN/MgO, respectively. Furthermore, the M - T data in both ZFC and FC protocols are separated thus confirming the presence of flux pinning in the films.^[27,28] In order to rule out the possibility of substrate-induced superconductivity, M - T measurements of bare substrates (Figure S3a,b, Supporting Information) are performed, showing no signs of super-

conductivity. The higher T_c for the MN/MgO film as compared to MN/Al₂O₃ is associated with the compressive in-plane strain.^[29] Two-step superconducting transitions (inset of Figure 2a,b) commonly arise from applied forces such as pressure, magnetic fields, strain, and proximity effects, and are observed in several other thin films as well.^[30–32] The temperature dependence of resistivity above the T_c (9–200 K) is analysed using the Bloch Grüneisen (BG) model,^[33] by taking account of the e - ph interactions. The fitting of the resistivity data (Figure S4, Supporting Information) strongly suggests that e - ph interactions are the dominant scattering mechanism for Mo₂N thin films.^[34] The e - ph coupling strength, estimated using McMillan's relation^[35] with a Coulomb pseudopotential $\mu^* = 0.13$, is found to be ≈ 0.75 for MN/Al₂O₃ and ≈ 0.76 for MN/MgO (Section SD, Supporting Information). This result highlights the enhancement of e - ph interactions due to compressive strain in MN/MgO compared to the tensile strain in MN/Al₂O₃.

Low-temperature magnetoresistance measurements (Figure 3a,b) revealed an increasing T_c width with applied magnetic field, which is a characteristic signature of type-II superconductors.^[36] The upper critical field H_{c2} , is estimated using the T_c^{onset} criterion, with the normal state resistance taken at ≈ 6.1 K, and by fitting the data with the Ginzburg-Landau (GL) model with an extrapolation to determine the $H_{c2}(0)$ for both films. According to the GL model, the critical field at a temperature, T is given by

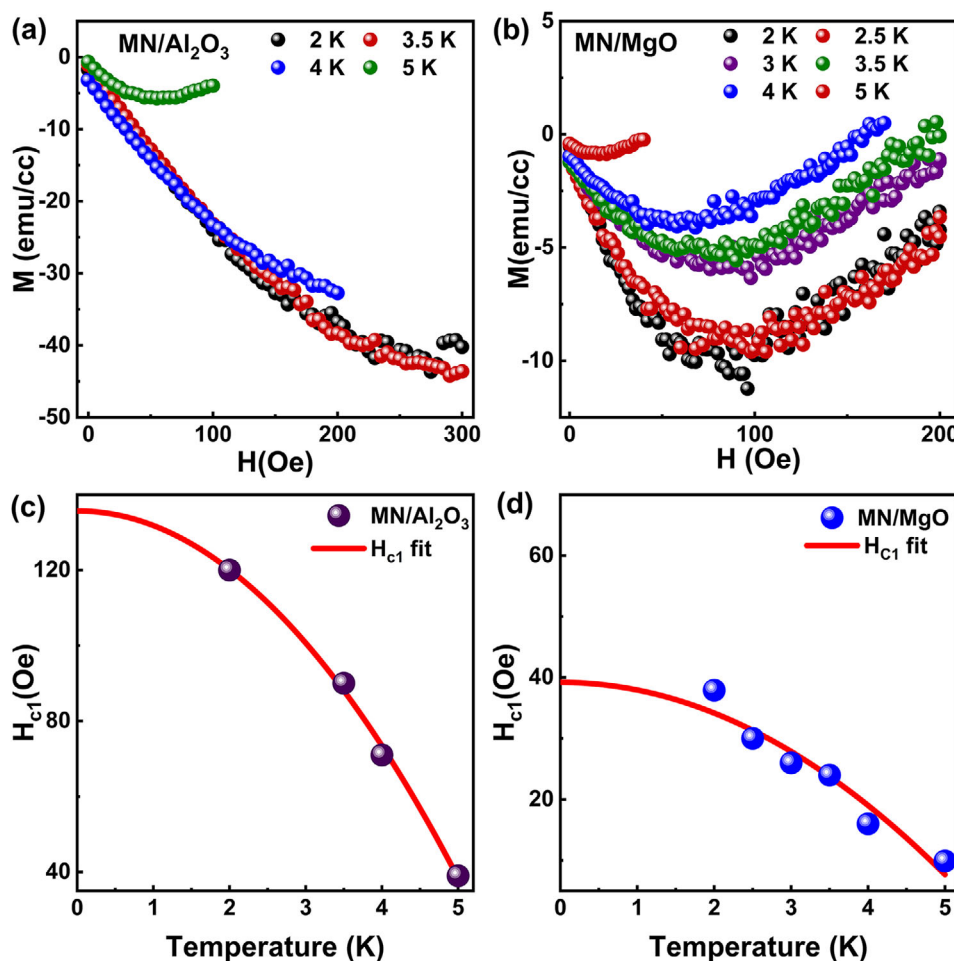


Figure 4. M - H plots (a,b) and H_{c1} versus T (c,d) plots of MN/Al_2O_3 and MN/MgO , respectively.

$H_{c2}(T) = H_{c2}(0) \frac{(1-t^2)}{(1+t^2)}$, where t is the reduced temperature given by $t = \frac{T}{T_c}$ and $H_{c2}(0)$ is upper critical field at 0 K. Based on this model, the estimated $H_{c2}(0)$ is found to be ≈ 5.1 T for MN/Al_2O_3 , and ≈ 7 T for MN/MgO , which is more than 25% enhancement in the MN/MgO than MN/Al_2O_3 .

The enhancements are attributed to the increased flux pinning potential resulting from a compressive in-plane strain on MN/MgO in contrast with the tensile in-plane strain in MN/Al_2O_3 , and also correlate with enhanced e - ph interactions.^[23,37,38] To understand further the nature of the superconductivity and the limiting mechanism of the Cooper pair formation, it is important to dive deeper into the mechanism governing H_{c2} . For this, the Werthamer–Helfand–Hohenberg (WHH) formula $H_{c2}^{orb}(0) = -0.693 T_c \left(\frac{dH_{c2}}{dT} \right)_{T=T_c}$,^[39] is used for estimation of the zero-temperature orbital limited upper critical field, $H_{c2}^{orb}(0)$. The calculated values are ≈ 4.4 T for MN/Al_2O_3 and ≈ 5.8 T for MN/MgO . These estimates are lower than the $H_{c2}(0)$ estimated from GL fitting. In general, the upper limit on H_{c2} is given by the Pauli Paramagnetic limit, which is given by $H_p = 1.86 T_c$ (9.6 T for MN/Al_2O_3 and 10.3 T for MN/MgO). The estimation and analysis clearly indicates a conventional

BCS-type superconductivity.^[40] To understand the mechanisms of Cooper pair breaking in type-II superconductors under an applied magnetic field, both orbital and spin-paramagnetic effects on the H_{c2} are considered. According to the Maki theory, the Maki parameter (α), which quantifies the relative strength of these effects, is defined as $\alpha = \sqrt{2} \frac{H_{c2}^{orb}(0)}{H_p(0)}$,^[41] The α values are found to be ≈ 0.64 (for MN/Al_2O_3) and ≈ 0.8 (MN/MgO), both less than 1, confirming that the superconductivity in Mo_2N thin films is limited by orbital depairing mechanisms. The GL coherence length (ξ_{GL}), is calculated by $\xi_{GL} = \sqrt{\frac{\phi_0}{2\pi H_{c2}(0)}}$, where $\phi_0 = 2.068 \times 10^{-15} \text{ T}\cdot\text{m}^2$ is magnetic flux quantum. The coherence length is found out to be ≈ 8.01 and ≈ 6.85 nm for MN/Al_2O_3 and MN/MgO films, respectively.

In order to estimate the H_{c1} of the samples, we have used the Meissner–Ochsenfeld criterion on the M - H measurements below T_c (Figure 4a,b).^[42] The obtained H_{c1} at different temperatures is analysed using the equation

$$H_{c1} = H_{c1}(0) \left[1 - \left(\frac{T}{T_c} \right)^2 \right] \quad (1)$$

Table 1. Superconducting parameters of MN/Al₂O₃ and MN/MgO.

Sample	Thickness [nm]	T_c [K]	$H_{c1}(0)$ [Oe]	$H_{c2}(0)$ [T]	$H_{c2}^{orb}(0)$ [T]	H_c [Oe]	ξ_{GL} [nm]	λ [nm]	α
MN/Al ₂ O ₃	130–135	5.18	135	5.12	4.37	1469	8.01	197	0.64
MN/MgO	130–135	5.57	39	6.98	5.83	814	6.85	416	0.8

where $H_{c1}(0)$ is lower critical field at 0 K. The obtained $H_{c1}(0)$ values for MN/Al₂O₃ and MN/MgO are found to be ≈ 135 and ≈ 39 Oe, respectively. Further, we have estimated the superconducting penetration depth (λ_{GL}) by $H_{c1} = \frac{\phi_0}{4\pi\lambda_{GL}^2} \ln(\frac{\lambda_{GL}}{\xi_{GL}})$, and λ_{GL} is found to be ≈ 197 and ≈ 416 nm for MN/Al₂O₃ and MN/MgO, respectively. The GL parameter (κ_{GL}) given by $\kappa_{GL} = \frac{\lambda_{GL}}{\xi_{GL}}$ is found to be ≈ 24.6 and ≈ 60.7 for MN/Al₂O₃ and MN/MgO, respectively. The values are much greater than $\frac{1}{\sqrt{2}}$, indicating a strong type-II superconductivity. To assess the superconducting condensation energy, the thermodynamic critical field (H_c) is evaluated using the relation $H_{c1}(0)H_{c2}(0) = H_c^2 \ln \kappa_{GL}$ and found to be ≈ 1469 Oe for MN/Al₂O₃ and ≈ 814 Oe for MN/MgO. All the characteristic superconducting parameters for both thin films are tabulated in **Table 1**.

Considering both $H_{c1}(T)$ and $H_{c2}(T)$ for the films, the superconducting phase diagram is presented in **Figure 5a,b**, showing distinct superconducting, intermediate, and normal states. The detailed analysis of the phase diagram confirms the thin films to be a strong type-II superconductor. These findings highlight the potential of Mo₂N thin films for integration into next-generation superconducting quantum and power electronic devices.

3. Conclusion

In summary, a significant enhancement of $\approx 25\%$ in the $H_{c2}(0)$ of MN/MgO is attributed to *e-ph* modulation arising from compressive in-plane strain, which enhances flux-pinning potential and overall superconducting performance compared to the tensile-strained MN/Al₂O₃. These findings demonstrate the crucial role and impact of strain engineering in tuning the superconducting behavior of transition metal nitride thin films. In comparison with earlier studies where improvements in H_{c2} were primarily

achieved through external pressure, chemical doping, or disorder engineering, our work establishes substrate-induced intrinsic strain as a clean and effective pathway for tuning superconductivity in transition metal nitride thin films. The results highlight strain engineering as a powerful alternative to conventional approaches, with the additional advantage of being compatible with scalable epitaxial growth. Looking ahead, the current system can be further optimized by selecting substrates with larger lattice mismatches, which are expected to induce stronger intrinsic strain effects. Complementary routes such as controlled doping, post-growth annealing, and thickness-dependent growth strategies could also be employed to fine-tune the carrier density, crystallinity, and pinning landscape, thereby pushing the superconducting performance even further. This work paves the way for their application in kinetic inductance devices, superconducting qubits, and miniaturization of superconducting interconnects for next-generation electronic technologies, highlighting the significant impact of strain on the superconducting properties of Mo₂N films.

4. Experimental Section

Thin Film Deposition: Molybdenum nitride thin films were grown on sapphire (Al₂O₃ (0001)) and MgO (111) substrates, by DC reactive magnetron sputtering in an ultrahigh vacuum chamber.^[43] Before deposition, the MgO substrates were cleaned by multiple sonication cycles first in i) a Hellmanex soap solution (≈ 3 mins), followed by ii) deionized water (two times for ≈ 5 mins), iii) acetone (≈ 10 mins), iv) ethanol (≈ 10 mins), and finally dried with compressed nitrogen gas.^[44] This procedure helps in the removal of possible hydroxides and carbonates present on the surface. The substrates were kept in the deposition chamber and evacuated to a pressure of $\sim 8.9 \times 10^{-9}$ Torr and the substrate temperature was kept at $\approx 500^\circ$ C. The deposition of Mo₂N was carried out with a mixture of Argon and Nitrogen (flow rates of Ar ≈ 22 sccm and N₂ ≈ 33 sccm).

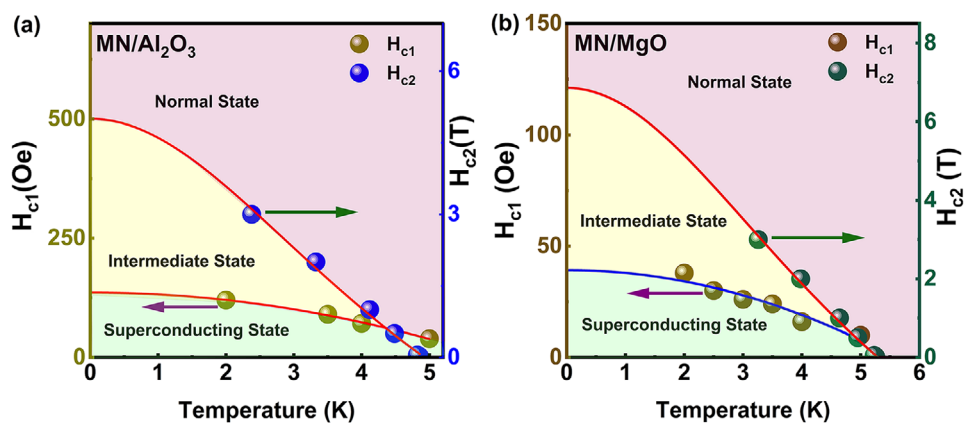


Figure 5. Phase diagram showing the superconducting, intermediate, and normal state of the a) MN/Al₂O₃, b) MN/MgO. Note: To distinguish between H_{c1} and H_{c2} , we have chosen two independent y axes.

Characterisation Studies: The compositions of the films were determined by ToF-ERDA using ≈ 36 MeV $^{127}\text{I}^{9+}$ ions as a probing beam with an incidence angle $\approx 67.5^\circ$, and a recoil angle $\approx 45^\circ$.^[45] The data were analysed using the Potku code.^[46] The crystal structure was investigated by XRD using a PANalytical X'Pert Pro diffractometer in Bragg-Brentano geometry and equipped with a $\text{Cu K}\alpha$ source operated at ≈ 45 kV and ≈ 40 mA. The incident optics had a $\approx 0.5^\circ$ divergence slit and a 0.5° anti-scatter slit, and the diffracted optics included a ≈ 5.0 mm anti-scatter slit, a 0.04 rad Soller slit, a Ni-filter, and an X'Celerator detector measuring in $\approx 0.008^\circ$ step sizes with an equivalent counting time of ≈ 19 s per step. For XRR, the PANalytical X'Pert Pro diffractometer was operated in line-mode with a hybrid mirror module with $\approx 0.5^\circ$ divergence slit for incident optics and a $\approx 0.125^\circ$ divergence slit for the diffracted optics. For the pole figure, the instrument was operated in point-mode with a crossed-slit module set at 2×2 mm as incident optics, and a $\approx 0.27^\circ$ parallel plate collimator for diffracted optics. Scanning electron microscopy (SEM) was performed using a Zeiss Sigma 300 with the field emission gun was operated at 2 kV. The atomic force microscopy (AFM) images of the films were taken using Bruker Dimension Icon AFM.

Physical and Magnetic Properties Measurements: The low-temperature electrical transport properties were performed using the physical property measurement system (PPMS, Quantum Design make). The temperature-dependent magnetization measurements were carried out using an MPMS3 SQUID-VSM magnetometer (Quantum Design make). In the zero-field-cooled (ZFC) protocol, the sample was first cooled from room temperature down to ≈ 2 K in the absence of an external magnetic field, and the magnetization was recorded during the subsequent warming cycle in the presence of a ≈ 5 Oe field. For the FC measurement, the sample was cooled in the presence of the same constant external magnetic field, and the magnetization was recorded continuously during this cooling process.

Supporting Information

Supporting Information is available from the Wiley Online Library or from the author.

Acknowledgements

A.S. acknowledges IIT Mandi for research facilities and DST India for Indo-Sweden bilateral grant (Grant No. DST/INT/SWD/VR/P-18/2019). P.E. acknowledges funding from the Swedish Government Strategic Research Area in Materials Science on Functional Materials at Linköping University (Faculty Grant SFO-Mat-LiU No. 2009 00971), the Knut and Alice Wallenberg Foundation through the Wallenberg Academy Fellows program (KAW-2020.0196, P.E.), and the Swedish Research Council (VR) under Project No. 2021-03826. A.M. and S.B. thank the Department of Atomic Energy (DAE), Government of India, for the financial support.

Conflict of Interest

The authors declare no conflict of interest.

Data Availability Statement

The data that support the findings of this study are available from the corresponding author upon reasonable request.

Keywords

DC magnetron sputtering, molybdenum nitride, strain engineering, superconductivity

Received: June 25, 2025

Revised: August 20, 2025

Published online: September 15, 2025

- [1] A. Engel, A. Aeschbacher, K. Inderbitzin, A. Schilling, K. Il'in, M. Hofherr, M. Siegel, A. Semenov, H.-W. Hübers, *Appl. Phys. Lett.* **2012**, *100*, 062601.
- [2] J. del Valle, J. G. Ramírez, M. J. Rozenberg, I. K. Schuller, *J. Appl. Phys.* **2018**, *124*, 211101.
- [3] Y. Zou, Q. Jin, Y. Wang, K. Jiang, S. Wang, Y. Li, E.-J. Guo, Z. G. Cheng, *Phys. Rev. B* **2022**, *105*, 224516.
- [4] Y. Zhou, W. Guo, T. Li, *Ceram. Int.* **2019**, *45*, 21062.
- [5] S. A. Rasaki, B. Zhang, K. Anbalgam, T. Thomas, M. Yang, *Prog. Solid State Chem.* **2018**, *50*, 1.
- [6] R. Ningthoujam, N. Gajbhiye, *Prog. Mater. Sci.* **2015**, *70*, 50.
- [7] E. Isaev, R. Ahuja, S. Simak, A. Lichtenstein, Y. K. Vekilov, B. Johansson, I. Abrikosov, *Phys. Rev. B* **2005**, *72*, 064515.
- [8] S. Wang, D. Antonio, X. Yu, J. Zhang, A. L. Cornelius, D. He, Y. Zhao, *Sci. Rep.* **2015**, *5*, 13733.
- [9] L. M. Corliss, N. Elliott, J. M. Hastings, *Phys. Rev.* **1960**, *117*, 929.
- [10] Q. Jin, H. Cheng, Z. Wang, Q. Zhang, S. Lin, M. A. Roldan, J. Zhao, J.-O. Wang, S. Chen, M. He, C. Ge, C. Wang, H.-B. Lu, H. Guo, L. Gu, X. Tong, T. Zhu, S. Wang, H. Yang, K.-J. Jin, E.-J. Guo, *Adv. Mater.* **2021**, *33*, 2005920.
- [11] X.-J. Chen, V. V. Struzhkin, Z. Wu, M. Somayazulu, J. Qian, S. Kung, A. N. Christensen, Y. Zhao, R. E. Cohen, H.-K. Mao, R. J. Hemley, *Proc. Natl. Acad. Sci. USA* **2005**, *102*, 3198.
- [12] (Ed: S. T. Oyama), *The Chemistry of Transition Metal Carbides and Nitrides*, 1st ed., Springer Netherlands, Dordrecht **1996**, pp. 1–27.
- [13] Y. Zhong, X. Xia, F. Shi, J. Zhan, J. Tu, H. J. Fan, *Adv. Sci.* **2016**, *3*, 1500286.
- [14] N. Kokubo, B. Gerekhuu, *Appl. Phys. Lett.* **2024**, *124*, 262601.
- [15] D. Zhang, Y. Pan, G. Wu, S. Yu, X. Zhong, Y. Wang, X. Liu, L. Wu, W. Peng, L. Zhang, L. Chen, Z. Wang, *Supercond. Sci. Technol.* **2023**, *36*, 125003.
- [16] N. Tureson, M. Marteau, T. Cabioch, N. Van Nong, J. Jensen, J. Lu, G. Greczynski, D. Fournier, N. Singh, A. Soni, L. Belliard, P. Eklund, A. le Febvrier, *Phys. Rev. B* **2018**, *98*, 205307.
- [17] L. Stöber, J. P. Konrath, V. Haberl, F. Patocka, M. Schneider, U. Schmid, *J. Vac. Sci. Technol., A* **2016**, *34*, 021513.
- [18] N. Haberkorn, S. Bengio, S. Suárez, P. D. Pérez, M. Sirena, J. Guimpel, *Mater. Lett.* **2018**, *215*, 15.
- [19] K. Inumaru, K. Baba, S. Yamanaka, *Appl. Surf. Sci.* **2006**, *253*, 2863.
- [20] N. Haberkorn, S. Bengio, H. Troiani, S. Suárez, P. D. Pérez, P. Granell, F. Golmar, M. Sirena, J. Guimpel, *Mater. Chem. Phys.* **2018**, *204*, 48.
- [21] M. Kuzmiak, M. Kopčík, F. Košuth, V. Vaňo, P. Szabó, V. Latyshev, V. Komanický, P. Samuely, *J. Supercond. Novel Magn.* **2022**, *35*, 1775.
- [22] J. Bekaert, C. Sevik, M. V. Milošević, *Nanoscale* **2020**, *12*, 17354.
- [23] M. Abrecht, D. Ariosa, D. Cloetta, S. Mitrovic, M. Onellion, X. X. Xi, G. Margaritondo, D. Pavuna, *Phys. Rev. Lett.* **2003**, *91*, 057002.
- [24] P. Stampe, M. Bullock, W. Tucker, R. J. Kennedy, *J. Phys. D: Appl. Phys.* **1999**, *32*, 1778.
- [25] R. Li, J. S. Gandhi, R. Pillai, R. Forrest, D. Starikov, A. Bensaoula, *J. Cryst. Growth* **2014**, *404*, 1.
- [26] Z. Dai, A. Miyashita, S. Yamamoto, K. Narumi, H. Naramoto, *Thin Solid Films* **1999**, *347*, 117.
- [27] X. Bai, F. Chen, Y. Wang, J. Xu, R. Zhang, M. Qin, W. Cheng, J. Zhang, Q. Shi, X. Wang, B. Zhu, J. Yuan, Q. Chen, J. Kang, K. Jiang, J. Hu, Y. Li, K. Jin, Z. Zhao, *Phys. Rev. Mater.* **2023**, *7*, 094801.
- [28] R. Jha, B. Tiwari, P. Rani, H. Kishan, V. P. S. Awana, *J. Appl. Phys.* **2014**, *115*, 213903.
- [29] F. Nabeshima, Y. Imai, M. Hanawa, I. Tsukada, A. Maeda, *Appl. Phys. Lett.* **2013**, *103*, 172602.
- [30] B. Wang, K. Matsubayashi, Y. Uwatoko, K. Ohgushi, *J. Phys. Soc. Jpn.* **2015**, *84*, 104706.
- [31] I. Pentin, Y. Vakhtomin, V. Seleznev, K. Smirnov, *Sci. Rep.* **2020**, *10*, 16819.

- [32] A. K. Verma, R. Gupta, S. Prakash, A. Gloskovskii, S. Kalal, P. Tiwari, V. R. Reddy, R. Rawat, M. Gupta, *ACS Appl. Electron. Mater.* **2024**, *6*, 5029.
- [33] J. M. Ziman, *Electrons and phonons: the theory of transport phenomena in solids*, Oxford University Press, Oxford, England **2001**.
- [34] A. Bid, A. Bora, A. K. Raychaudhuri, *Phys. Rev. B* **2006**, *74*, 035426.
- [35] W. L. McMillan, *Phys. Rev.* **1968**, *167*, 331.
- [36] A. S. Ilin, A. O. Strugova, I. A. Cohn, V. V. Pavlovskiy, S. V. Zaitsev-Zotov, A. V. Sadakov, O. A. Sobolevskiy, L. A. Morgun, V. P. Matrovitskii, G. V. Rybalchenko, *Phys. Rev. Mater.* **2024**, *8*, 074801.
- [37] T. Horide, T. Maekawa, T. Aikawa, T. Kitamura, K. Nakamura, *Phys. Rev. Mater.* **2024**, *8*, 094802.
- [38] R. Zhang, X. Li, F. Meng, J. Bi, S. Zhang, S. Peng, J. Sun, X. Wang, L. Wu, J. Duan, H. Cao, Q. Zhang, L. Gu, L.-F. Huang, Y. Cao, *ACS Appl. Mater. Interfaces* **2021**, *13*, 60182.
- [39] N. R. Werthamer, E. Helfand, P. C. Hohenberg, *Phys. Rev.* **1966**, *147*, 295.
- [40] A. M. Clogston, *Phys. Rev. Lett.* **1962**, *9*, 266.
- [41] K. Maki, *Phys. Rev.* **1966**, *148*, 362.
- [42] M. Falkowski, Z. Śniadecki, T. J. Bednarchuk, A. Kowalczyk, *J. Appl. Phys.* **2023**, *133*, 243901.
- [43] A. Le Febvrier, L. Landälv, T. Liersch, D. Sandmark, P. Sandström, P. Eklund, *Vacuum* **2021**, *187*, 110137.
- [44] A. Le Febvrier, J. Jensen, P. Eklund, *J. Vac. Sci. Technol., A* **2017**, *35*, 021407.
- [45] M. Mayer, S. Möller, M. Rubel, A. Widdowson, S. Charisopoulos, T. Ahlgren, E. Alves, G. Apostolopoulos, N. P. Barradas, S. Donnelly, S. Fazinic, K. Heinola, O. Kakuee, H. Khodja, A. Kimura, A. Lagoyannis, M. Li, S. Markelj, M. Mudrinic, P. Petersson, I. Portnykh, D. Primetzhofer, P. Reichart, D. Ridikas, T. Silva, S. M. Gonzalez de Vicente, Y. Q. Wang, *Nucl. Fusion* **2019**, *60*, 025001.
- [46] K. Arstila, J. Julin, M. I. Laitinen, J. Aalto, T. Konu, S. Kärkkäinen, S. Rahkonen, M. Raunio, J. Itkonen, J.-P. Santanen, T. Tuovinen, T. Sajavaara, *Nucl. Instrum. Methods Phys. Res. Section B: Beam Interactions with Materials and Atoms* **2014**, *331*, 34.